Nanoscale

Dynamic Article Links

Cite this: *Nanoscale*, 2011, **3**, 4840

www.rsc.org/nanoscale

PAPER

Hybrid A–B–A type nanowires through cation exchange†

A. K. Samal and T. Pradeep*

Received 18th August 2011, Accepted 11th September 2011
DOI: 10.1039/c1nr11124h

Hybrid A–B–A type nanowires (NWs) with Ag_5Te_3–HgTe–Ag_5Te_3 composition have been created by the reaction of Hg^{2+} with Ag_2Te NWs. The NW morphology of Ag_2Te is preserved upon reaction with minor changes and the two separate phases formed are spatially separated within the same NW. The reaction of Hg^{2+} with Ag_2Te NWs was monitored at different concentrations and the reactivity was attributed to cationic exchange depending on solubility products. Hybrid NWs were formed by partial cation exchange only at low concentrations (below 50 ppm) resulting in Ag_5Te_3 and HgTe within the same NW. However, at high concentrations (above 100 ppm), the HgTe phase alone was formed. These studies have been extended to other metal ions such as Pb^{2+}, Cd^{2+}, and Zn^{2+} whose reactivity towards Ag_2Te NWs is different from that of Hg^{2+}. These ions form a passivating Te oxide layer upon reaction with other metal ions. The mechanism of reactivity of Hg^{2+} is explained on the basis of free energy of formation of the ionic solid. Phase transition of Hg^{2+}-reacted NWs occurs at a lower temperature than the parent (Ag_2Te NWs) and other metal ions-reacted Ag_2Te NWs. Details of the process were elucidated using microscopic and spectroscopic investigations. The physical and chemical properties of the individual components within a NW are expected to provide a novel functionality to the metal chalcogenide systems.

Introduction

Anisotropic nanomaterials,[1] especially one-dimensional nanostructures such as nanorods[2–4] and nanowires,[5–7] are important in diverse areas. Applications of NWs in areas such as electronics,[8] solar cells,[9] sensors,[10] and single electron transistors[11] have been intensely pursued. However, hybrid NWs containing multiple phases within the same structure are more attractive as they enhance the functionality of the materials and provide novel properties in comparison to the parent systems as in the case of Te–Se–Te NWs.[12] Silver telluride nanowires (Ag_2Te NWs)[13–16] are important as this material in its bulk form is an interesting semiconductor with a narrow band gap of 0.04–0.17.[17] It exhibits a phase transition from a low temperature monoclinic structure (β-Ag_2Te) to a high temperature cubic structure (α-Ag_2Te) at ~418 K.[18,19] The β-Ag_2Te phase shows high mobility of electrons in the monoclinic lattice whereas the α-Ag_2Te phase shows high mobility of Ag^+ in the face-centered cubic lattice.[13,20] It is suggested that the silver ions move between the neighboring tetrahedral sites *via* an octahedral site.[20,21] The concentration of electrons decreases in Ag_2Te by a factor of 4 as a result of phase transition from β-Ag_2Te to α-Ag_2Te.[22] It has also been reported that non-stoichiometric Ag_2Te composition exhibits large positive magnetoresistance.[23–25] Similarly, Ag^0–Ag_2Te composite exhibits electrical bistability at low voltages, wherein two distinct conducting states are observed.[26] Ag_2Te is known to show thermoelectric property and a higher value of Seebeck coefficient was observed for Ag_2Te NWs than bulk and thin films.[14] A huge magnetoresistance and higher Seebeck coefficient were observed under a magnetic field of 7 T.[27] Surface enhanced Raman scattering (SERS) of Ag_2Te NWs was studied using crystal violet (CV) as the analyte and a sensitivity up to 10^{-7} M of CV was observed.[15] Combining tellurides with diverse properties within the same NW structure is exciting from their aforementioned properties.

The subject area of chemical reactivity of metal chalcogenides has grown significantly in the recent past.[28–36] To illustrate the rapid expansion of the area with the example of silver chalcogenides, we note that several detailed reports of their reactions with Cd^{2+}, Pb^{2+}, Zn^{2+}, Pt^{2+}, and Pd^{2+} have appeared.[29–36] It has been conclusively established that reactions of metal ions with ionic chalcogenides proceeds through a cation-exchange mechanism, wherein the progress of reaction is dependent on the free energy of formation of the product, which can be assessed from the solubility product (K_{sp}) of the reactants and the products. Cationic exchange occurs in the ionic solid with a relatively high K_{sp} value to form another ionic solid with a relatively low

DST Unit of Nanoscience (DST UNS), Department of Chemistry, Indian Institute of Technology Madras, Chennai, 600 036, India. E-mail: pradeep@iitm.ac.in; Fax: +91-44-2257-0545/0509

† Electronic supplementary information (ESI) available: XRD, SEM, TEM, and TEM-EDAX of Hg^{2+}-reacted Ag_2Te NWs. TEM of other metal ions-reacted Ag_2Te NWs. Plot of concentration of Hg^{2+} *versus* Ag^+ and Hg^{2+} in the supernatant. DSC of Ag_2Te NWs. XPS data of metal ions-reacted Ag_2Te NWs. XRD of Hg^{2+}-reacted Ag_2Te NWs previously reacted with Zn^{2+}. See DOI: 10.1039/c1nr11124h

K_{sp}. Additives or complexing agents such as trioctylphosphine (TOP) or tributylphosphine (TBP) were used to increase the solubility of the ions without increasing the solubility product, as the complexed species do not take part in the solubility equilibrium.[35] The temperature also plays a vital role in the solubility product. An increase in temperature increases the solubility for an endothermic reaction. It has also been established that due to changes in the crystallinity of the material post-reaction, nanostructured materials undergo severe mechanical stress leading to changes in morphology and dimensions.[37,38] Taniguchi *et al.* suggested that the cation exchange is triggered by a difference in the redox potentials of the reacting species.[39,40] In the present study, two important aspects of chemical reactivity of ionic chalcogenides have been focused upon: (i) intermediate species and the hybrid structures formed during cation exchange reaction (with Hg^{2+}) and (ii) surface analysis of the ionic chalcogenides when reacted with metal ions, wherein cation exchange reactions are infeasible under normal conditions.

The first aspect focuses on understanding the state of equilibrium for a cationic exchange reaction, *i.e.*, reaction products during an incomplete transformation. A typical cationic exchange reaction, $M^{2+} + Ag_2Te \rightleftarrows MTe + 2Ag^+$, produces a stoichiometric product. However, it is important to understand whether Ag^+ escapes from the chalcogenide network immediately or whether the reaction proceeds through the formation of intermediary species. Several possibilities exist for the intermediate steps during the progress of the reaction. For example, in the case of Hg^{2+}, the possibilities include gradual stoichiometric replacement of Ag^+ with Hg^{2+}, formation of Ag–Hg bimetallic chalcogenide and formation of multiphasic systems. In the previously studied reactions between metal ions and ionic chalcogenides,[33,35] the difference in the solubility products of reactant and product was so large that the cation exchange reaction was extremely facile (*e.g.*, Pt^{2+} with CdS, K_{sp} (CdS) $= 1 \times 10^{-28}$, K_{sp} (PtS) $= 9.9 \times 10^{-74}$). In the present study, in order to understand the intermediate products formed during the reaction, the concentration of the metal ion was kept low for an incomplete cation exchange reaction. The products after complete reaction were also investigated.

The second aspect of our investigation focuses on understanding the surface reactivity of ionic chalcogenides with metal ions, wherein cation exchange reaction is thermodynamically infeasible at room temperature. It has been understood from the previous studies that the progress of such reactions is highly dependent on the presence of complexation agents and temperature.[31,41,42] Without the use of a complexation agent and at room temperature, the composition of the parent chalcogenide nanostructure remains intact. However, there are a few important questions still unanswered regarding the infeasibility of such reactions at room temperature. Does the surface of the parent chalcogenide particle remain intact as its bulk? Or are there reactions occurring at the chalcogenide surface? In order to answer these questions, we studied the chalcogenide surface upon reaction with metal ions spectroscopically.

Experimental section

Sodium dodecyl sulfate (SDS, $C_{12}H_{25}O_4SNa$, 99%) was obtained from Acros. Tellurium dioxide (TeO_2, 99.9%) powder was purchased from Alfa Aesar. Silver nitrate ($AgNO_3$) and hydrazine monohydrate ($N_2H_4 \cdot H_2O$, 99–100%) were purchased from SD Fine Chemicals, India. All the metal salts such as mercuric acetate ($Hg(CH_3CO_2)_2$), lead acetate ($Pb(CH_3CO_2)_2$), cadmium acetate ($Cd(CH_3CO_2)_2$), and zinc acetate ($Zn(CH_3CO_2)_2$) were purchased from Merck, India. To avoid anion effects, we used acetates throughout. Deionized water was used throughout the experiment.

Ag_2Te NWs was synthesized at room temperature using Te NWs as templates as in the case of other tellurides.[15,43,44] Synthesis of Ag_2Te was carried out in two steps. In the first step, Te NWs were prepared by the chemical method; originally, reported by Chang *et al.*[45] In a typical procedure, 160 mg of TeO_2 powder was slowly added to a beaker containing 100 mL of hydrazine monohydrate. The reaction was allowed to continue at room temperature under constant stirring. The powder was completely dissolved and the color of the solution changed from colorless to blue after 1 h. Blue color indicates the formation of Te NWs. After 1 h, the solution was diluted 10-fold with 10 mM SDS, in order to control the length of the NWs. The as-prepared solution was purified by centrifugation at 35 000*g* for 10 min, in order to remove excess hydrazine and SDS. The residue was redispersed in deionized water and centrifuged twice for the complete removal of unreacted species. In the second step, 100 mL of $AgNO_3$ (10 mM) was added to 900 mL of the purified Te NWs and stirred for 12 h. The color of the solution changed from blue to black. The solution was centrifuged at 35 000*g* for 10 min, and the process was repeated twice for the complete removal of unreacted species.

The reactivity of transition metal ions was studied by the addition of metal salts such as $Hg(CH_3CO_2)_2$, $Pb(CH_3CO_2)_2$, $Cd(CH_3CO_2)_2$, and $Zn(CH_3CO_2)_2$ to the purified Ag_2Te NWs separately. Calculated amounts of metal ions were added into the Ag_2Te NW solution to make the final concentration of metal ions as 10 ppm. Concentrations used were low so that activity was not different from concentration. The reaction mixture was stirred for 24 h. Thereafter, the reaction mixture was centrifuged twice at 35 000*g* for 10 min and the residue was re-dispersed in deionized water for characterization. Further, a few experiments were conducted to understand the metal ion concentration dependent reactivity by the sequential addition of the same ion to increase its concentration. All studies were carried out with samples after reaction with 10 ppm metal ions, unless otherwise stated. The residue obtained after centrifugation was freeze-dried for further studies.

Instrumentation

High-resolution transmission electron microscopy (HRTEM) was performed with a JEOL 3010, 300 kV instrument equipped with a UHR polepiece. Energy dispersive X-ray analysis (EDAX) was carried out with an Oxford EDAX housed in the TEM. Samples were prepared by dropping the dispersion on carbon coated copper grids and drying in ambient conditions. Scanning electron microscopy (SEM) was carried out using an FEI QUANTA-200 SEM instrument and the samples were prepared on conducting ITO glass plates. X-Ray diffraction (XRD) data were collected with a Bruker AXS, D8 Discover diffractometer using Cu-K_α ($\lambda = 1.54$ Å) radiation. Samples were

scanned in the 2θ range from 10–90°. All the peaks were assigned and compared with the database published by the Joint Committee on Powder Diffraction Standards (JCPDS). Differential scanning calorimetry (DSC) was carried out using a NETZSCH DSC 204 instrument under nitrogen atmosphere, at a heating rate of 10 K per minute. X-Ray photoelectron spectroscopy (XPS) measurements were done using an Omicron ESCA Probe spectrometer with polychromatic Mg-K_α X-rays ($h\nu = 1253.6$ eV). Raman spectra were recorded using a WiTec GmbH confocal micro-Raman equipped with a charge coupled device (CCD) detector. The light source was a frequency doubled Nd:YAG laser of 532 nm wavelength.

Results and discussion

All peaks in the XRD pattern of the parent Ag_2Te NWs (Fig. 1) are indexed to the monoclinic phase whose unit cell parameters calculated from diffraction peaks are, $a = 0.8185$ nm, $b = 0.8934$ nm, $c = 0.8418$ nm, and $\beta = 113.7°$, which are consistent with the literature data (JCPDS: 34-0142). The NWs appear well formed with 600 ± 50 nm in length and 20 ± 4 nm in width as seen in the TEM image A (inset of Fig. 1). No particles or other shapes were present. The NWs are single crystalline and a high resolution image of the body of a single NW is shown in B (inset of Fig. 1). The (220) plane is clear in the image and it extends from one end to the other of the NW. The structure of Ag_2Te NWs is similar to the parent Te NWs and no defects were observed. The NWs show Ag and Te in 2 : 1 atomic ratio justifying the assignment (inset of Fig. 1A).

The structural integrity of Ag_2Te NWs is explained by the close lattice match between hexagonal Te NWs and monoclinic Ag_2Te NWs. Typically during the addition of metal ions into the parent chalcogen, the NWs are observed to undergo volumetric transformations of various forms, resulting in breaking and bending of NWs.[33] However, it is well understood that the preparation of silver chalcogenides from chalcogen under moderate conditions does not affect the single crystallinity of the structure and surface defects are not introduced.[35]

Upon reaction with Hg^{2+}, NWs underwent comprehensive structural changes resulting in new features (Fig. 2). The assignment of peaks suggests the presence of two phases in the NWs after the reaction: cubic HgTe (JCPDS: 75-2084), marked in red and other peaks (green), assigned to hexagonal Ag_5Te_3 (JCPDS: 16-0372). From XRD we do not know whether two distinct NWs or particles of these two phases exist in the system.

A large area TEM image of Hg^{2+}-reacted Ag_2Te NWs (at 10 ppm) is shown in the inset of Fig. 2. Upon the addition of Hg^{2+}, Ag_2Te NWs undergo aggregation and form bundles. Note that the formation of the bundle occurs without any complexation agent and heat treatment. All these reactions were carried out in water and at room temperature. HRTEM images of individual NWs were studied carefully. Stacking faults were observed upon reaction with Hg^{2+} (Fig. S1A†). It is known that planar defects such as stacking faults are readily formed in the NWs during crystal growth with low stacking fault energy.[46,47] These arise due to the stabilization of the surfaces, which exhibit higher energy and need fast growth in a particular direction.[48,49] The inset of Fig. S1A† shows the expanded view of stacking faults. The presence of such defects during cation exchange was reported earlier.[33,35] The pristine Ag_2Te NWs have no defects as seen in HRTEM (inset of Fig. 1). HgTe is cubic in nature whereas Ag_5Te_3 is hexagonal. The inherent difference in the crystal structures of the two chalcogenides can lead to stacking fault in the NWs. The observed interplanar distance of 0.48 nm corresponds to the (201) plane of Ag_5Te_3. Although the HgTe lattice is not seen in this image, there are other regions on the grid where the (111) plane of HgTe is seen (see below). This is also seen when the Hg^{2+} concentration is higher in the reaction.

To understand the nature of two phases, HgTe and Ag_5Te_3 in the Hg^{2+}-reacted NWs, elemental mapping was carried out. EDAX images of a single NW are shown in Fig. 3. While Te is

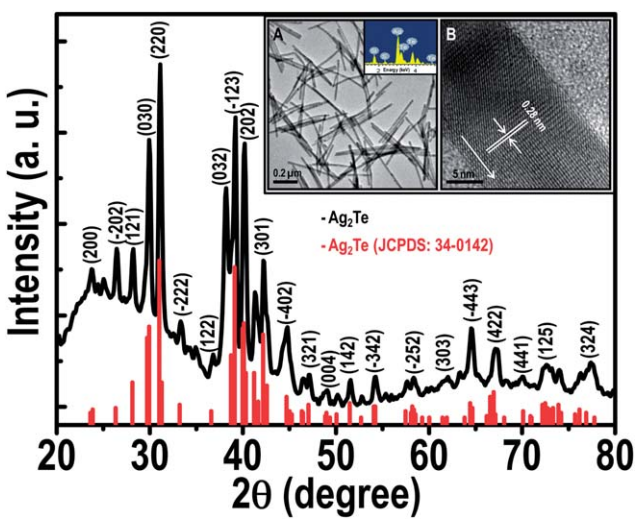

Fig. 1 XRD patterns of Ag_2Te NWs (black trace). All peaks are indexed to monoclinic Ag_2Te. Standard peaks of Ag_2Te (JCPDS: 34-0142) are given as the stick spectrum. The inset shows (A) large area TEM of Ag_2Te NWs and (B) HRTEM image of the body of a single Ag_2Te NW showing the (220) plane. The inset of inset A shows the EDAX spectrum of Ag_2Te NWs.

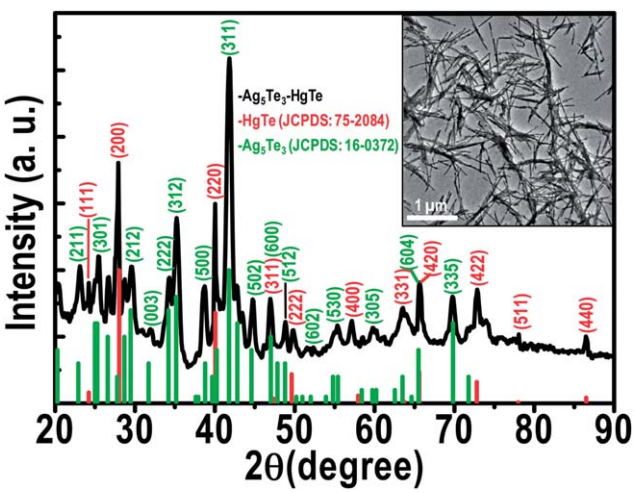

Fig. 2 XRD pattern of Hg^{2+}-reacted Ag_2Te NWs (black trace). Peaks labeled red are from cubic HgTe and those labeled in green are assigned to hexagonal Ag_5Te_3. The expected peaks of the two phases, HgTe (JCPDS: 75-2084) and Ag_5Te_3 (JCPDS: 16-0372) are shown as sticks. The inset shows a large area TEM image of Hg^{2+}-reacted Ag_2Te NWs.

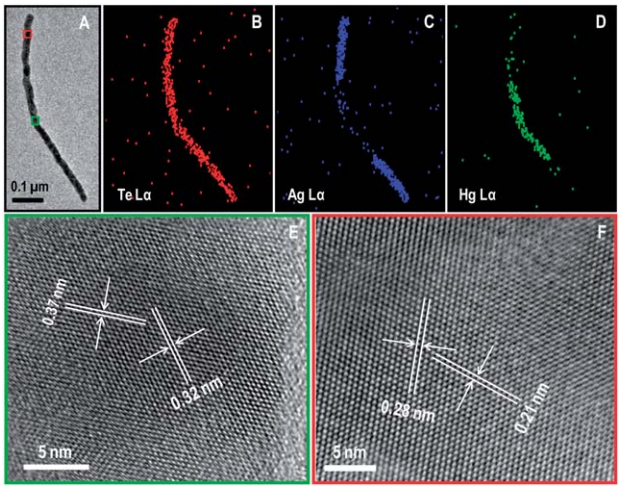

Fig. 3 TEM image used for the elemental mapping and HRTEM (A), elemental mapping of Te (B), Ag (C), Hg (D), HRTEM images of HgTe (E) and Ag_5Te_3 (F) phases, collected from the green and red rectangles marked in (A).

present all through the NW, Ag and Hg are present at specific locations. Interestingly, where Hg is present, Ag is absent and *vice versa* (Fig. 3B–D). It is observed that the HgTe phase is present (confirmed from high resolution data) where Hg is detected. Similarly the presence of Ag indicates the Ag_5Te_3 phase. It is also observed that hybrid structures got slightly distorted in some of the places.

Further confirmation of the phases comes from HRTEM analysis. Fig. 3A shows the TEM image used for elemental mapping and corresponding HRTEM images. HRTEM of Hg present (green rectangle) and absent (red rectangle) regions of a single NW are shown in Fig. 3E and F. The interplanar distances 0.32 and 0.37 nm in Fig. 3E correspond to (200) and (111) planes of cubic HgTe, respectively. HRTEM image of Ag rich phase (red rectangle) is shown in Fig. 3F. The interplanar distances 0.21 and 0.28 nm correspond to (331) and (003) planes of hexagonal Ag_5Te_3, respectively. The images indicate that both HgTe and Ag_5Te_3 phases exist in a single NW confirming the existence of hybrid structures.

The presence of such biphasic NWs were observed throughout the samples. Large area elemental maps of the bundles of Hg^{2+}-reacted Ag_2Te NWs (Fig. 4) showed that Hg was not present throughout the NWs. As mentioned before, in large area TEM, bundles are seen. Fig. 4A shows a large area TEM image used for elemental mapping. In the portion where Hg was present (indicated by a green box), Ag was absent (indicated by a red box) in the NW bundles and *vice versa*. There are also a few other places where Hg is absent while Te and Ag are present in the same nanostructure (indicated by a white box in the TEM). Thus, it appears that monophasic Ag_5Te_3 NWs are also present. However, the concentration of such NWs is low. As the mutually exclusive regions of Hg and Ag (marked with boxes) are larger than the dimensions of isolated NWs, it appears that there is some self-organization of individual phases. However, in most regions, the widths of the HgTe and Ag_5Te_3 regions are shorter than the resolution of elemental maps and therefore the intensities are smeared.

The atomic ratio of Hg to Ag to Te obtained from quantitative analysis of Hg Lα, Ag Lα and Te Lα in the EDAX spectrum of the bundles is ~2 : 9 : 11. It appears that compositional inhomogeneity as seen in the large area elemental images is the reason for the observed ratio. Before the reaction, the atomic ratio of Ag : Te was ~2 : 1 corresponding to Ag_2Te. A large area SEM and a single bundle of Hg^{2+}-reacted Ag_2Te NWs show similar morphology as observed in TEM (Fig. S1B†).

The reactivity of other metal ions such as Pb^{2+}, Cd^{2+}, and Zn^{2+} with Ag_2Te NWs were studied. Ag_2Te NWs do not undergo any structural changes and all the planes are indexed to the parent Ag_2Te NWs (Fig. 5) upon reaction with other metal ions. Large area and HRTEM images of other metal ions-reacted Ag_2Te NWs (at 10 ppm) are shown in Fig. S2†. No stacking faults are observed for other metal ions-reacted NWs; however, the surface concentration of Te(IV) has increased. It is likely that this surface oxide prevents the diffusion of cations and subsequent formation of exchange products (see later). Elemental analysis of metal ions-reacted Ag_2Te NW bundles was done using TEM-EDAX. Elemental analysis is expected to give an understanding of the extent of metal ion present in Ag_2Te NWs. The results show variation in the reactivity of metal ions with Ag_2Te NWs.

After Hg^{2+} reaction, it is detected in the bundle and Ag : Te ratio decreased significantly. However, for other metal ions-reacted Ag_2Te NWs, the concentrations of metal ions in the bundle are almost negligible and the ratios of Ag : Te are almost unaffected. Thus for Hg^{2+}, the Ag content in the bundle decreased significantly presumably due to Ag^+ dissolution. However, in the case of reaction of other metal ions, the concentrations of these metals are negligible. The atomic ratios of Pb^{2+}, Cd^{2+}, and Zn^{2+}-reacted Ag_2Te NWs are as follows: Pb : Ag : Te = 0.60 : 16.00 : 7.00, Cd : Ag : Te = 0.03 : 10.60 : 5.00, and Zn : Ag : Te = 0.15 : 11.50 : 7.00.

In the synthetic procedure, the Ag content in the Ag_2Te suspension corresponds to 216 ppm (1 mM). Therefore, 10 ppm Hg^{2+} (0.05 mM) is inadequate for complete cation exchange. This is true for other metal ions too. Thus the reaction of Hg^{2+} with Ag_2Te NWs at low concentration occurs through a partial cation exchange resulting in hybrid structures. The resulting Ag^+ dissolves in solution whereas Hg^{2+} forms HgTe. Depending on the concentration of Hg^{2+}, the extent of Ag^+ dissolution can be controlled. However, at higher concentrations, the reactivity was different. We studied higher concentrations such as 100 and 1000 ppm of Hg^{2+}. At these concentrations of Hg^{2+} (100 and 1000 ppm), XRD patterns of the post-reaction residue showed the formation of predominantly cubic HgTe (JCPDS: 75-2084) (Fig. S3†). The NW structure is preserved during this transformation. Large area TEM and HRTEM images of the product are shown in Fig. S4†. As can be seen, the length and width of NWs are not affected significantly. HRTEM image shows the interplanar distances of 0.18 and 0.15 nm corresponding to (222) and (400) planes of cubic HgTe. Elemental mapping of Hg^{2+} (1000 ppm) reacted Ag_2Te shows a complete absence of Ag in the NW (Fig. S5†). The atomic ratio of Hg : Te is close to 1 : 1. Thus we can conclude that at a higher concentration of Hg^{2+}, complete cation exchange occurs and HgTe is formed. In contrast, incomplete cation exchange in Hg^{2+}-reacted Ag_2Te NWs leads to Te excess within the NW. Instead of forming mixed AgHgTe NWs, phase separation occurs within the NW, resulting in HgTe

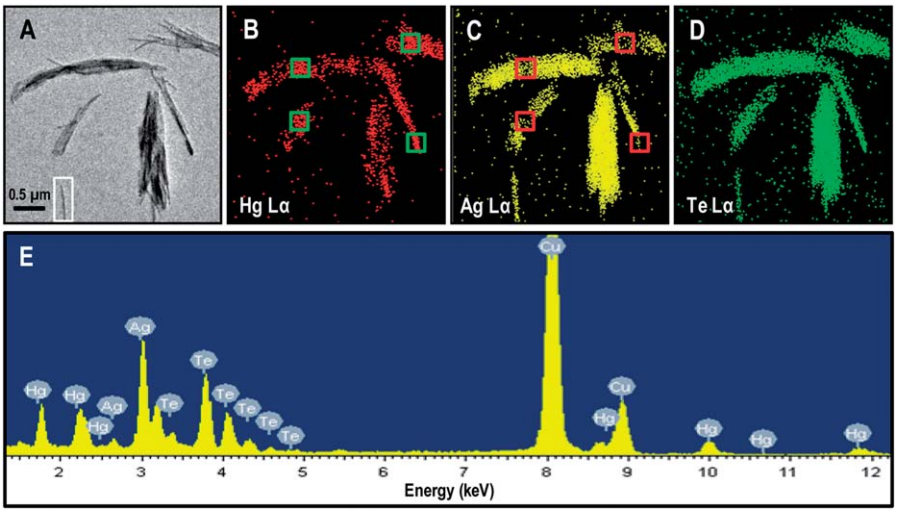

Fig. 4 TEM image used for the elemental mapping (A), elemental mapping of Hg (B), Ag (C) and Te (D), and EDAX spectrum (E) of Hg^{2+}-reacted Ag_2Te NWs. Cu was from the substrate used for the measurement.

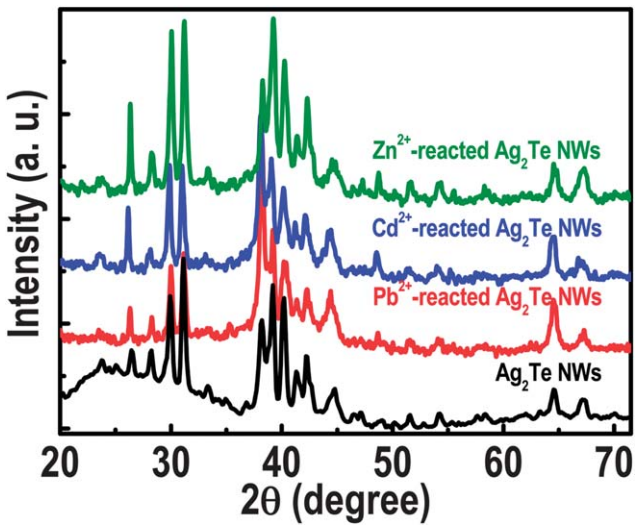

Fig. 5 A comparison of the XRD patterns of metal ions-reacted Ag_2Te NWs and the parent NWs.

and Ag_5Te_3 phases. Note that Ag_2Te and Ag_5Te_3 are the low temperature stoichiometric phases in the Ag–Te system[50,51] and therefore, this transformation is not unexpected. It is also known that Ag_2Te thin films transform slowly to stable Ag_5Te_3 in the presence of excess Te.[52] Thus, the cation exchange reactions observed are

$$5Ag_2Te + 2Hg^{2+} \rightarrow Ag_5Te_3 + 2HgTe + 5Ag^{+} \text{ (low concentration of } Hg^{2+}) \quad (1)$$

$$Ag_2Te + Hg^{2+} \rightarrow HgTe + 2Ag^{+} \text{ (high concentration of } Hg^{2+}) \quad (2)$$

Reaction (1) is not charge-balanced. It appears that Ag_5Te_3 may be mixed valent in Te to account for it. However, we did not find any literature on mixed valency in this system. As NWs are biphasic, a clear distinction of the possible Te states is not seen in XPS (see below).

Removal of Ag^{+} by Hg^{2+} in Ag_2Te NWs was studied by ICP-OES at different concentrations of Hg^{2+}. Table 1 shows the dissolution of Hg, Ag and Te ions observed after the reaction with Hg^{2+}. It was observed that with increase in the concentration of Hg^{2+}, the concentration of Ag^{+} in the supernatant increases, implying the replacement of Ag^{+} by Hg^{2+} and the formation of HgTe. The concentrations of Ag^{+} and Hg^{2+} in the supernatant are plotted against the input concentration of Hg^{2+} (Fig. S6†). A linear plot implies ionic substitution. As the ratio of Ag^{+} to Hg^{2+} is nearly constant in both the concentration regimes (reactions (1) and (2)), it is difficult to see a distinct change in slope with the concentration of Hg^{2+} added. Note that we observed a negligible amount of Te in the supernatant.

The cation-exchange reaction in chalcogenides is dependent on three parameters, namely, solubility of the parent chalcogenide vis-à-vis the exchange product, crystal structure and volume change during the reaction. Thermodynamic feasibility of the exchange reaction can be established based on the solubility product of the reactants and products ($\Delta G = -RT \ln K_{sp}$). Concentrations may be used to evaluate K_{sp} at low solute concentrations. The reaction proceeds when the reactant has high K_{sp} and the product obtained after cation exchange has low K_{sp}. This leads to favorable Gibbs' free energy change for the reaction. Typically, the solubility of a species can be influenced by a number of factors, *e.g.*, temperature, common ion effect, presence of a complexing agent, solvent polarity and particle size. A compilation of solubility products of various metal chalcogenides was reported by Xia *et al.*[35] and the data of relevance are shown in Table 2.

The solubility products of all metal chalcogenides of relevance are not available in the literature;[33] however, conclusions may be drawn based on the following general feature. It is known that the solubility products of metal chalcogenides decrease as the ionic radius of the chalcogen increases *i.e.* K_{sp} (M_xS_y) > K_{sp} (M_xSe_y) > K_{sp} (M_xTe_y).[35] This is true for M_xS_y and M_xSe_y and it is expected that metal tellurides will show the same trend. It is also known that cationic exchange occurs when an ionic solid product has lower solubility than a reactant. Based on the

Table 1 The amount of Hg, Ag and Te ions obtained from the supernatant after reaction with Hg^{2+} (BDL: below detection limit, 0.05 ppm)

Sample	Ag_2Te	$Hg_{initial}$/ppm	Hg_{final}/ppm	$Ag_{solution}$/ppm	$Te_{solution}$/ppm
1	1 mM, 10 mL	5	0.05	2.24	BDL
2	1 mM, 10 mL	10	0.53	6.38	BDL
3	1 mM, 10 mL	25	1.47	18.48	BDL
4	1 mM, 10 mL	50	3.08	42.48	0.62
5	1 mM, 10 mL	100	7.20	87.80	1.29

Table 2 Solubility product data of various metal chalcogenides. NA refers to data 'not available'

Solid	E = S	E = Se	E = Te
Ag_2E	3×10^{-50}	1×10^{-54}	NA
HgE	6×10^{-53}	4×10^{-59}	NA
PbE	1×10^{-28}	1×10^{-37}	NA
CdE	1×10^{-28}	4×10^{-35}	1×10^{-42}
ZnE	3×10^{-25}	1×10^{-27}	NA

solubility data, a feasible exchange reaction is possible between Hg^{2+} and Ag_2Te whereas other metal ions (Pb^{2+}, Cd^{2+}, and Zn^{2+}) can't react with Ag_2Te at normal reaction conditions.

Structural phase transitions of Ag_2Te NWs after reaction with metal ions were studied. It is known that Ag_2Te shows a structural phase transition from the low temperature monoclinic structure (β-Ag_2Te) to the high temperature cubic structure (α-Ag_2Te).[15,18,19,27] The DSC data of NWs pre- and post-reaction were measured under nitrogen atmosphere at a heating/cooling rate of 10 K per minute. For Ag_2Te NWs, a sharp peak was observed at 417.7 K (Fig. S7†),[15] indicative of the endothermic structural phase transition from the monoclinic to face centered cubic phase, observed during heating. During cooling, an exothermic peak centered at 403.9 K was observed, attributed to the reverse transition. Kinetics of the cubic to the monoclinic transition is known to be slower than the reverse, explaining the broad DSC feature.

For metal ions-reacted Ag_2Te NWs, the phase transitions varied with the metal ion (Fig. 6). In the case of Hg^{2+}-reacted NWs, a substantial change in the phase transition temperature was observed. The transitions during heating and cooling were observed at 379.2 and 367.9 K (a and a′). However, in the case of other metal ions, the heating and cooling curves were similar to that of the parent NWs [Pb^{2+}: 415.9 and 402.2 K (b and b′); Cd^{2+}: 415.9 and 403.5 K (c and c′); Zn^{2+}: 418.1 and 402.4 K (d and d′)]. The data are summarized in Table 3. Lowering of phase transition temperature of Hg^{2+}-reacted Ag_2Te NWs is in accordance with the hybrid nature of the NW formed at low concentration of Hg^{2+}. It is known that bulk HgTe shows a phase transition at high pressure.[53,54] Bulk Ag_5Te_3 does not show a phase transition in the window investigated whereas a transition at 378 K in the Ag_2Te system at excess Te was observed earlier.[50,51]

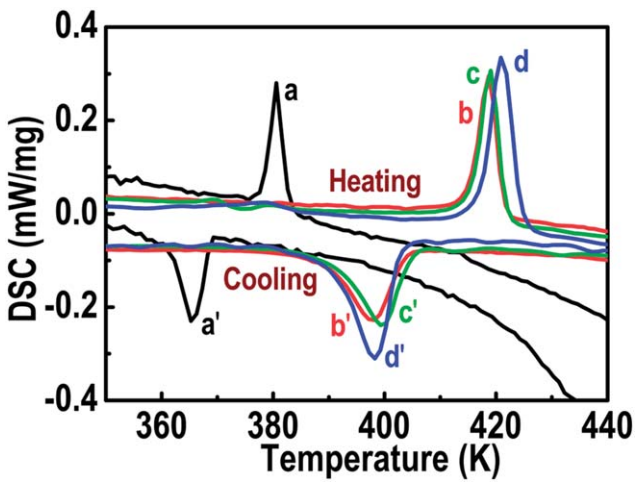

Fig. 6 DSC curves of Hg^{2+} (a and a′), Pb^{2+} (b and b′), Cd^{2+} (c and c′), and Zn^{2+} (d and d′) reacted Ag_2Te NWs.

Metal ions-reacted Ag_2Te NWs were studied by XPS. Expanded spectra in the Te 3d region of metal ions-reacted Ag_2Te NWs are shown in Fig. 7. The peaks of Te $3d_{5/2}$ and Te $3d_{3/2}$ for all the metal ions-reacted Ag_2Te are almost at the same binding energies (Te $3d_{5/2}$ = 572.3 and Te $3d_{3/2}$ = 582.7 eV). Along with the two main tellurium peaks, two other peaks are observed at higher binding energies, which can be attributed to Te(IV) oxide. The XPS spectrum of Te(IV) is similar to those reported previously.[55,56] XPS spectra in the Te 3d region of Hg^{2+}, Pb^{2+}, Cd^{2+}, and Zn^{2+}-reacted Ag_2Te NWs are shown in B, C, D, and E, respectively in Fig. 7. For comparison, the expanded spectrum in the Te 3d region of parent Ag_2Te NWs is given in Fig. 7A. The concentration of Te(IV) on the surface of NWs was increased as we move from Hg^{2+} to Zn^{2+}. In the case of Hg^{2+}-reacted NWs, the intensity has increased slightly and for Zn^{2+} it was much higher. The peak at 572.3 eV is due to Te $3d_{5/2}$ and a low-intensity peak at 575.3 eV is due to Te(IV). The XPS spectrum in the Hg 4f region of the corresponding sample (Fig. S8A†) shows a peak at 99.8 eV, due to Hg $4f_{7/2}$ of metal chalcogenide (HgTe). The corresponding Pb 4f region shows a peak at 137.9 eV assigned to Pb $4f_{7/2}$ (Fig. S9A†). The peak at 404.6 eV is due to Cd $3d_{5/2}$ (Fig. S10A†). Similarly, the peak at 1021.2 eV is due to Zn $2p_{3/2}$ (Fig. S11A†). The Ag 3d region is given along with each reacting metal in respective figures. No significant change is seen in the Ag 3d region. All the exposed metals exist in the divalent state.

Binding energies of Ag_2Te and metal ions-reacted Ag_2Te NWs are tabulated in Table 4. Thus, the XPS analysis of Ag_2Te NW bundles reveals that M^{2+} exist on the NW surface wherein the concentration of Te(IV) has also increased in comparison to the parent Ag_2Te NWs. It is expected that the metal ion incorporation happens largely at the surface of the NWs as the bulk properties (such as DSC and XRD) are similar to parent Ag_2Te NWs. As mentioned, the cation exchange reaction is thermodynamically hindered. It is suggested that M^{2+} ions interact with the NW surfaces leading to bundling of the NWs.

Table 3 Phase transition temperatures of metal ions-reacted Ag_2Te NWs

Sample/phase transition	Parent Ag_2Te	Hg^{2+}-reacted Ag_2Te	Pb^{2+}-reacted Ag_2Te	Cd^{2+}-reacted Ag_2Te	Zn^{2+}-reacted Ag_2Te
Heating/K	417.7	379.2	415.9	415.9	418.1
Cooling/K	403.9	367.9	402.2	403.5	402.4

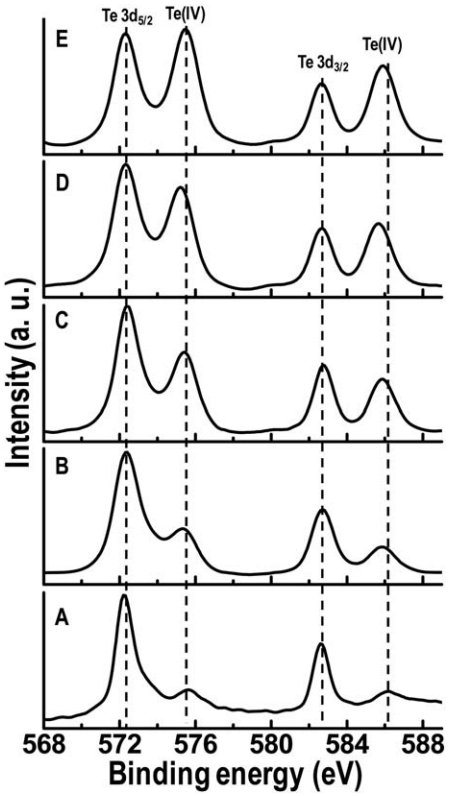

Fig. 7 The expanded XPS spectra in the Te 3d region of Hg^{2+} (B), Pb^{2+} (C), Cd^{2+} (D), and Zn^{2+} (E) reacted Ag_2Te NWs. For comparison the Te 3d region of Ag_2Te is given in (A).

The increase in the concentration of Te(IV) on the surface of NW was studied by Raman spectroscopy. Fig. 8 compares the Raman spectra of metal ions-reacted Ag_2Te NW with the parent sample. Two prominent peaks are observed at 484 (±2) and 723 (±3) cm^{-1} along with a small peak at 332 (±4) cm^{-1}.

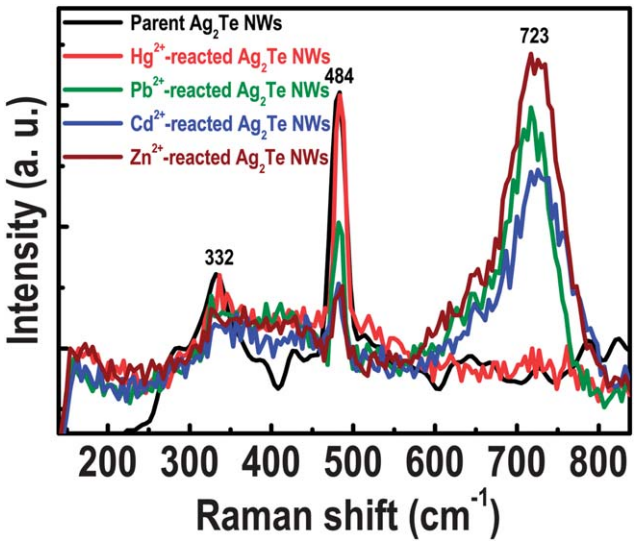

Fig. 8 Raman spectra of metal ions-reacted Ag_2Te NWs.

All the peaks are relevant to the oxidation state of Te. The peak at 332 cm^{-1} is assigned to the bending vibration of $[TeO_3]^{2-}$.[55] The peak at 484 cm^{-1} is present in the parent Ag_2Te NWs and is attributed to the presence of Te–O bending vibration of the oxide layer.[57] The peak at 723 cm^{-1}, which is absent in the parent as well as Hg^{2+}-reacted Ag_2Te NWs, can be assigned to the stretching vibration of the TeO_3 trigonal pyramid. With the increasing concentration of $[TeO_3]^{2-}$, this peak intensity is enhanced.[58] It is known that Ag_2Te is sensitive to laser beams, which can induce a redox reaction.[18,59] Upon the exposure of laser on the surface of Ag_2Te, trace amounts of TeO_2 and silver are formed.[18] After interacting with metal ions, Te undergoes oxidation and the oxygen content increases, which is evident from the peak at 723 cm^{-1}. This surface oxidation is absent in Hg^{2+}-reacted Ag_2Te NWs.

Table 4 Details of the binding energies of Ag_2Te and metal ions-reacted Ag_2Te NWs

Ag_2Te/metal ions-reacted Ag_2Te	Reacted metal/eV	Silver/eV	Tellurium/eV	Te(IV)/eV
Ag_2Te	Nil	Ag $3d_{5/2}$ = 368.2, $3d_{3/2}$ = 374.2	Te $3d_{5/2}$ = 572.3, $3d_{3/2}$ = 582.6	Te $3d_{5/2}$ = 575.6, $3d_{3/2}$ = 586.1
Hg^{2+}-reacted Ag_2Te	Hg $4f_{7/2}$ = 99.8, $4f_{5/2}$ = 103.9	Ag $3d_{5/2}$ = 368.1, $3d_{3/2}$ = 374.1	Te $3d_{5/2}$ = 572.3, $3d_{3/2}$ = 582.7	Te $3d_{5/2}$ = 575.3, $3d_{3/2}$ = 585.9
Pb^{2+}-reacted Ag_2Te	Pb $4f_{7/2}$ = 137.9, $4f_{5/2}$ = 142.7	Ag $3d_{5/2}$ = 367.9, $3d_{3/2}$ = 373.9	Te $3d_{5/2}$ = 572.4, $3d_{3/2}$ = 582.7	Te $3d_{5/2}$ = 575.4, $3d_{3/2}$ = 585.8
Cd^{2+}-reacted Ag_2Te	Cd $3d_{5/2}$ = 404.6, $3d_{3/2}$ = 411.3	Ag $3d_{5/2}$ = 368.1, $3d_{3/2}$ = 374.1	Te $3d_{5/2}$ = 572.3, $3d_{3/2}$ = 582.7	Te $3d_{5/2}$ = 575.2, $3d_{3/2}$ = 585.7
Zn^{2+}-reacted Ag_2Te	Zn $2p_{3/2}$ = 1021.2, $2p_{1/2}$ = 1044.3	Ag $3d_{5/2}$ = 368.0, $3d_{3/2}$ = 374.0	Te $3d_{5/2}$ = 572.3, $3d_{3/2}$ = 582.7	Te $3d_{5/2}$ = 575.4, $3d_{3/2}$ = 585.9

The reaction of metal ions with Te(IV) formed on the NW surface was studied. In this experiment, Hg^{2+} (10 ppm) was added to Zn^{2+}-reacted Ag_2Te NWs. The expectation was that the presence of Te(IV) on the surface of Zn^{2+}-reacted Ag_2Te NWs would prevent the cation exchange reaction even for Hg^{2+}. The XRD pattern of the residue obtained after reaction between Hg^{2+} (10 ppm) and Zn^{2+}-reacted Ag_2Te NWs is shown in Fig. S12†. XRD features match exactly with the parent Ag_2Te NWs. This clearly suggests that Hg^{2+} is unable to penetrate the NWs due to the presence of a passivating oxide layer.

Conclusions

Cation exchange in Ag_2Te NWs with Hg^{2+}, Pb^{2+}, Cd^{2+}, and Zn^{2+} at several metal ion concentrations, especially in the range of incomplete exchange, was investigated in detail. The reactivity of Hg^{2+} with Ag_2Te is significantly different from the other metal ions and the products were hybrid structures. At lower concentration of Hg^{2+}, Ag_5Te_3 and HgTe were observed in a single NW, whereas only HgTe was observed at higher concentrations. An increase in Ag^+ concentration was detected in the solution as cation exchange occurred. The phase transition of Hg^{2+}-reacted NWs showed a lowering of temperature compared to the parent (Ag_2Te) as well as the other metal ions-reacted NWs. The surface concentration of Te(IV) increased significantly after reaction with Pb^{2+}, Cd^{2+}, and Zn^{2+} which was confirmed by surface analysis using XPS and Raman spectroscopy. The physical and chemical properties of the individual components within a NW are expected to provide a novel functionality to the metal chalcogenide systems.

Acknowledgements

We thank the Nano Mission of the DST, Government of India for supporting our research program.

References

1 P. R. Sajanlal, T. S. Sreeprasad, A. K. Samal and T. Pradeep, *Nano Rev.*, 2011, **2**, 5883, and the references cited therein.
2 J. Pérez-Juste, I. Pastoria-Santos, L. M. Liz-Marzán and P. Mulvaney, *Coord. Chem. Rev.*, 2005, **249**, 1870–1901.
3 C. J. Murphy, T. K. Sau, A. M. Gole, C. J. Orendorff, J. Gao, L. Gou, S. E. Hunyadi and T. Li, *J. Phys. Chem. B*, 2005, **109**, 13857–13870.
4 X. Huang, S. Neretina and M. A. El-Sayed, *Adv. Mater.*, 2009, **21**, 4880–4910.
5 Y. Xia, P. Yang, Y. Sun, Y. Wu, B. Mayers, B. Gates, Y. Yin, F. Kim and H. Yan, *Adv. Mater.*, 2003, **15**, 353–389.
6 M. Law, J. Goldberger and P. Yang, *Annu. Rev. Mater. Res.*, 2004, **34**, 83–122.
7 S. V. N. T. Kuchibhatla, A. S. Karakoti, D. Bera and S. Seal, *Prog. Mater. Sci.*, 2007, **52**, 699–913.
8 Y. Cui and C. M. Lieber, *Science*, 2001, **291**, 851–853.
9 B. Tian, X. Zheng, T. J. Kempa, Y. Fang, N. Yu, G. Yu, J. Huang and C. M. Lieber, *Nature*, 2007, **449**, 885–889.
10 L. Mu, W. Shi, J. C. Chang and S. T. Lee, *Nano Lett.*, 2008, **8**, 104–109.
11 C. Thelander, T. Martensson, M. T. Bjork, B. J. Ohlsson, M. W. Larsson, L. R. Wallenberg and L. Samuelson, *Appl. Phys. Lett.*, 2003, **83**, 2052–2054.
12 R. Chen, D. Xu, G. Guo and L. Gui, *J. Mater. Chem.*, 2002, **12**, 2435–2438.
13 T. P. Vinod, M. Park, S. H. Kim and J. Kim, *Langmuir*, 2010, **26**, 9195–9197.
14 F. Li, C. Hu, Y. Xiong, B. Wan, W. Yan and M. Zhang, *J. Phys. Chem. C*, 2008, **112**, 16130–16133.
15 A. K. Samal and T. Pradeep, *J. Phys. Chem. C*, 2009, **113**, 13539–13544.
16 F. Xiao, G. Chen, Q. Wang, L. Wang, J. Pei and N. Zhou, *J. Solid State Chem.*, 2010, **183**, 2382–2388.
17 W. Gorbachev, *Semiconductor Compounds $A_2^IB^{VI}$, Metallurgy*, Moscow, 1980.
18 A. M. Qin, Y. P. Fang, P. F. Tao, J. Y. Zhang and C. Y. Su, *Inorg. Chem.*, 2007, **46**, 7403–7409.
19 P. Gnanadurai, N. Soundararajan and C. E. Sooriamoorthi, *Phys. Status Solidi B*, 2003, **237**, 472–478.
20 M. Kobayashi, K. Ishikawa, F. Tachibana and H. Okazaki, *Phys. Rev. B*, 1988, **38**, 3050–3055.
21 T. Tomari, M. Kobayashi and H. Okazaki, *Solid State Ionics*, 1989, **35**, 355–358.
22 S. A. Aliev, Z. F. Agaev and E. I. Zulfigarov, *Semiconductors*, 2007, **41**, 1027–1032.
23 R. Xu, A. Husmann, T. F. Rosenbaum, M. L. Saboungi, J. E. Enderby and P. B. Littlewood, *Nature*, 1997, **390**, 57–60.
24 H. S. Schnyders, M. L. Saboungi and T. F. Rosenbaum, *Appl. Phys. Lett.*, 2000, **76**, 1710–1712.
25 I. S. Chuprakov and K. H. Dahmen, *Appl. Phys. Lett.*, 1998, **72**, 2165–2167.
26 S. K. Batabyal and J. J. Vittal, *Chem. Mater.*, 2008, **20**, 5845–5850.
27 Y. Sun, M. B. Salamon, M. Lee and T. F. Rosenbaum, *Appl. Phys. Lett.*, 2003, **82**, 1440–1442.
28 Z. H. Lin and H. T. Chang, *Langmuir*, 2008, **24**, 365–367.
29 D. H. Son, S. M. Hughes, Y. Yin and A. P. Alivisatos, *Science*, 2004, **306**, 1009–1012.
30 U. Jeong, J. U. Kim, Y. Xia and Z. Y. Li, *Nano Lett.*, 2005, **5**, 937–942.
31 U. Jeong, Y. Xia and Y. Yin, *Chem. Phys. Lett.*, 2005, **416**, 246–250.
32 P. H. C. Camargo, Y. H. Lee, U. Jeong, Z. Zou and Y. Xia, *Langmuir*, 2007, **23**, 2985–2992.
33 E. S. Wark, C. H. Hsia and D. H. Son, *J. Am. Chem. Soc.*, 2008, **130**, 9550–9555.
34 Q. Yao, I. U. Arachchige and S. L. Brock, *J. Am. Chem. Soc.*, 2009, **131**, 2800–2801.
35 G. D. Moon, S. Ko, Y. Xia and U. Jeong, *ACS Nano*, 2010, **4**, 2307–2319.
36 A. Dorn, P. M. Allen, D. K. Harris and M. G. Bawendi, *Nano Lett.*, 2010, **10**, 3948–3951.
37 L. Dloczik and R. Koenenkamp, *Nano Lett.*, 2003, **3**, 651–653.
38 X. C. Jiang, B. Mayers, Y. L. Wang, B. Cattle and Y. Xia, *Chem. Phys. Lett.*, 2004, **385**, 472–476.
39 S. Taniguchi, M. Green and T. Lim, *J. Am. Chem. Soc.*, 2011, **133**, 3328–3331.
40 S. Taniguchi and M. Green, *J. Mater. Chem.*, 2011, **21**, 11592–11598.
41 U. Jeong, P. H. C. Camargo, Y. H. Lee and Y. Xia, *J. Mater. Chem.*, 2006, **16**, 3893–3897.
42 J. M. Luther, H. Zheng, B. Sadtler and A. P. Alivisatos, *J. Am. Chem. Soc.*, 2009, **131**, 16851–16857.
43 A. K. Samal and T. Pradeep, *J. Phys. Chem. C*, 2010, **114**, 5871–5878.
44 A. K. Samal and T. Pradeep, *Langmuir*, 2010, **26**, 19136–19141.
45 Z. H. Lin, Z. Yang and H. T. Chang, *Cryst. Growth Des.*, 2008, **8**, 351–357.
46 H. W. Liang, S. Liu, Q. S. Wu and S. H. Yu, *Inorg. Chem.*, 2009, **48**, 4927–4933.
47 U. Dahmen, C. Hetherington, V. Radmilovic, E. Johnson, S. Xiao and C. Luo, *Microscopy and Microanalysis*, 2002, **8**, 247–256.
48 Y. Ding and Z. L. Wang, *J. Phys. Chem. B*, 2004, **108**, 12280–12291.
49 J. L. Elechiguerra, J. Reyes-Gasga and M. J. Yacaman, *J. Mater. Chem.*, 2006, **16**, 3906–3919.
50 E. A. Echmaeva and E. G. Osadchii, *Geol. Ore Deposits*, 2009, **51**, 247–258.
51 I. Karakaya and W. T. Thompson, *J. Phase Equilib.*, 1991, **12**, 56–63.
52 V. Simic and Z. Marinkovic, *Thin Solid Films*, 1979, **61**, 149–160.
53 J. Blair and A. C. Smith, *Phys. Rev. Lett.*, 1961, **7**, 124–125.
54 P. Grima, A. Polian, M. Gauthier, J. P. Itie, M. Mezouar, G. Weill, J. Besson, M. D. Hausermann and H. Hanfland, *J. Phys. Chem. Solids*, 1995, **56**, 525–530.
55 M. K. Bahl, R. L. Watson and K. J. Irgolic, *J. Chem. Phys.*, 1977, **66**, 5526.
56 J. M. Song, Y. Z. Lin, Y. J. Zhan, Y. C. Tian, G. Liu and S. H. Yu, *Cryst. Growth Des.*, 2008, **8**, 1902–1908.
57 R. L. Frost and E. C. Keeffe, *Spectrochim. Acta, Part A*, 2009, **73**, 146–149.
58 B. V. R. Chowdari and P. P. Kumari, *Mater. Res. Bull.*, 1999, **34**, 327–342.
59 G. Henshaw, I. P. Parkin and G. A. Shaw, *J. Chem. Soc., Dalton Trans.*, 1997, 231–236.